Geometrically nonlinear structural modal analysis using fictitious masses

Bernhammer, Lars O.; De Breuker, Roeland

DOI
10.2514/1.J054787

Publication date
2017

Document Version
Final published version

Published in
AIAA Journal

AIAA JOURNAL
Vol. 55, No. 10, October 2017

Geometrically Nonlinear Structural Modal Analysis Using Fictitious Masses

Lars O. Bernhammer* and Roeland De Breuker†
Delft University of Technology, 2629 HS Delft, The Netherlands
and
Moti Karpel‡
Technion—Israel Institute of Technology, 32000 Haifa, Israel

DOI: 10.2514/1.J054787

In this paper, a new method to obtain a geometrically nonlinear structural dynamics model based on the full linear finite element model of slender structures is presented. For this purpose, a finite element model is divided into multiple segments along its span. For each segment, a modal analysis is carried out. Boundary grid points are defined on each segment and loaded by fictitious masses. The modal analysis produces a set of elastic modes and six rigid-body modes that have significant deformations near the boundary. These deformations facilitate high-accuracy integration of the segments into a coupled model, in which the fictitious masses are removed. The elastic modes are used as master modes that describe the deformation, whereas the rigid-body modes are used as slave modes to establish displacement compatibility between the segments. The modal analysis is carried out with the local segment attached to its own reference frame, yielding a local linear solution that is part of a global nonlinear analysis. Large rotations and displacements are provided by the rigid-body modes in a corotational framework.

Nomenclature

$\boldsymbol{A}$	=	state matrix
$\boldsymbol{B}$	=	input matrix
$\bar{\boldsymbol{B}}$	=	generalized damping matrix
$\boldsymbol{C}$	=	output matrix
$\boldsymbol{D}$	=	feedthrough matrix
$\boldsymbol{e}$	=	unit vector of coordinate systems
$\boldsymbol{F}$	=	force vector
$\boldsymbol{f}_c$	=	vector of centrifugal force
$\boldsymbol{f}_g$	=	vector of gravitational force
$\boldsymbol{f}_\omega$	=	vector of rotational force
$\boldsymbol{g}$	=	gravity vector
$\boldsymbol{I}$	=	identity matrix
$\bar{\boldsymbol{K}}$	=	generalized stiffness matrix
$\bar{\boldsymbol{M}}$	=	generalized mass matrix
$\boldsymbol{M}_f$	=	mass matrix containing fictitious masses only
$\bar{\boldsymbol{M}}_f$	=	generalized mass matrix including fictitious masses
$\boldsymbol{m}$	=	vector containing concentrated masses
$\boldsymbol{n}$	=	number of modes per segment, number of segments
$\boldsymbol{R}$	=	rotation matrix
$\boldsymbol{r}$	=	position vector
$\boldsymbol{T}$	=	transformation matrix
$\boldsymbol{u}$	=	displacement vector
$\boldsymbol{u}_r$	=	rotation vector
ζ	=	damping-coefficient matrix
ξ_e	=	elastic-mode displacement
ξ_r	=	rigid-body mode displacement
τ	=	pseudotime
$\boldsymbol{\Phi}$	=	normal modes of a system with fictitious masses removed
ϕ	=	normal modes that serve as generalized coordinates
Ψ	=	rotation angle
ψ	=	rotation magnitude
$\boldsymbol{\Omega}$	=	rotation vector
ω	=	angular velocity
ω_n	=	natural frequency

Presented as Paper 2014-0715 at the 32nd ASME Wind Energy Symposium, National Harbor, MD, 13–17 January 2014; received 5 October 2015; revision received 9 April 2017; accepted for publication 4 August 2017; published online 11 September 2017.

*Ph.D. Candidate, Aerospace Structures and Computational Mechanics/Wind Energy.
†Assistant Professor, Aerospace Structures and Computational Mechanics.
‡Professor, Sanford Kaplan Chair for Aerospace Engineering. Fellow AIAA.

I. Introduction

AEROELASTIC simulations of aircraft and wind turbines are time consuming, certainly when including geometric nonlinearities in a high-fidelity structural model. Several software tools have been developed to model the wing and blade structure using either multibody formulations or beam models. One of the nonlinear beam formulations is the intrinsic beam model. A comprehensive overview of the beam theory is provided by Hodges [1]. Hodges [2] has first presented formulations that describe the strain–velocity relations. Inherently, beam models are one-dimensional models, combined with cross-sectional properties. Asymptotic methods can be used to obtain the stiffness and mass properties of a cross section of a slender beam [3,4]. Palacios and Palacios et al. obtained the cross-sectional properties based on a full linear finite element model [5,6], thereby matching the detail level from linear load models with nonlinear beam models. As the formulations are strain based, the rotations and displacements that are needed for an aerodynamic analysis need to be retrieved. Quaternions allow tracing the deformation by integrating the strains along the beam axis [6]. Several of the nonlinear beam models have been validated against the Princeton beam experiment, which is a cantilever beam with a large tip displacement. Hodges and Patil [7] compare this experiment to the intrinsic beam formulation; Dowell et al. [8] make a comparison with the Dowell–Hodges formulation; and Hopkins and Ormiston [9] benchmark their tool based on a combination of rigid- and flexible body kinematics, in which the flexibility is described by beam elements.

The second approach is the flexible multibody formulation, as incorporated in packages as MSC/Adams. Several different approaches are used in multibody codes. One approach uses rigid bodies that are interconnected by springs, which can only provide very coarse structural solutions. More advanced multibody codes use flexible elements, and are usually based on energy formulations [10] or beam formulations [11]. The element formulations are provided in a rotational framework. Shabana et al. [12] distinguish floating-frame approaches, incremental-rotation approaches, or

large-rotation vectors. The large-rotation-vector approach is used for the formulations in this paper. Most research predominantly focuses on beam formulations, as three-dimensional finite element models are computationally very costly for multibody simulations [13] and the effective introduction of constraints to those simulations [14,15]. This paper will present an alternative, compact formulation, based on modal reduction, for a full geometrically nonlinear simulation of slender structures.

The starting assumption is that the structural dynamics, for example, of a wind turbine, can be separated into substructures, such as the blades, the tower, and the drive train. These substructures can be further broken down into segments, for which modal reductions are carried out. The mode shapes and the generalized stiffness and mass matrices of the separate segments are then used as a basis for the analysis. Compatibility between two connected segments is established through displacement constraints applied to the rigid-body modes. The underlying assumption here is that large deformations and rotations are modeled by rigid-body modes in a corotational framework, whereas elastic modes serve as master coordinates for the deformations. Two intersegmental displacement-compatibility types can be identified. The first one is a fixed connection, in which the two sides of the connection have the same displacements and rotations. A geometrically nonlinear formulation is provided in this paper for this type of connection. An example would be the interface between multiple wing segments. The second type of connection allows relative rotational degrees of freedom between the segments. In the case of aircraft, morphing wings can be named. Selitrennik et al. [16] provide formulations for a morphing wing–body structure with a single rotational degree of freedom between the wing and body motions of a flight vehicle. A similar approach is used by De Breuker et al. [17], who developed a morphing-wing framework based on nonlinear beam formulations in a corotational framework.

The structural model can be seen as a geometrically nonlinear extension of the modal coupling method of Craig and Bampton [18]. Nonlinear compatibility is introduced between the different segments through rotation matrices. Additionally, the modal basis is obtained using fictitious masses [19]. This approach allows obtaining a set of rigid-body and elastic modes, which are close to a fixed–fixed condition in a single modal analysis, in which all modes are orthogonal, and so no orthogonalization procedure needs to be followed as in the case of the Craig–Bampton's approach. The modal basis can be used, as described in this paper, to model the dynamic structural response of a full wind turbine or a morphing aircraft.

II. Modeling Aspects

The modeling approach is an extension to a research program, in which modal-based formulations for geometrically nonlinear structural dynamics were investigated. Selitrennik et al. [16] have modeled morphing aircraft structures, using geometrically nonlinear compatibility relations. This paper describes two types of connections that can link segments to each other. A novel geometrically nonlinear structural model describes in detail how fixed connections between two adjacent subsegments can be formulated, for example, in the case of large wing deformations, in which the subsegments of the wing are linked to each other. The second type of joints is morphing connection, as described by Selitrennik et al. [16].

The modeling process starts with a standard modal analysis for each segment, performed with large fictitious masses loading the boundary coordinates. The resulting modes and generalized matrices are used to perform the subsequent simulations. Compatibility is established between the segments during the time-domain simulation in an iterative manner.

A. Fictitious Masses

For the modal analysis, each structural segment can be analyzed individually and is integrated into the global structural model through compatibility conditions for the boundary grid points of the segments. A full linear finite element model can be used, as will be shown in a numerical example, as a basis for such a modal reduction. For each segment, the boundary grid points are defined and loaded by large fictitious masses, which is a well-established method in substructuring [19,20]. At each of these boundary points, two or more segments will be connected with each other. Fictitious masses are concentrated inertia terms that need to be large enough to introduce significant local deformations near the connecting grid points of each segment. As such, their magnitudes should be typically larger than the respective inertia of the segment under consideration, but not too large to avoid numerical ill-conditioning [20]. As the analysis is performed with free–free boundary conditions, rigid-body modes and elastic modes with significant local deformations are obtained. For subsequent analyses, the fictitious masses need to be removed from the generalized mass matrix by

$$\bar{\boldsymbol{M}} = \bar{\boldsymbol{M}}_f - \boldsymbol{\phi}^T \boldsymbol{M}_f \boldsymbol{\phi} \tag{1}$$

in which $\bar{\boldsymbol{M}}_f$ is the generalized mass matrix of a segment with fictitious masses, and $\boldsymbol{M}_f$ has the same dimension as the full discrete mass matrix. Because only the boundary elements are loaded, the matrix containing the fictitious masses $\boldsymbol{M}_f$ is nonzero only for the nodal locations of the fictitious mass. $\boldsymbol{\phi}$ denotes the eigenvectors of the structure generated with fictitious masses. $\bar{\boldsymbol{M}}$ is the full generalized mass matrix of a segment to be used in the geometrically nonlinear analysis. The diagonal generalized stiffness matrix is not affected by the removal of the fictitious masses.

B. Equations of Motion

The basic assumption is that the structural displacements in each segment are defined by the sum of large rigid-body displacements and rotations of the local body-attached coordinate system and small elastic deformations. As an example, the displacements of two structural segments and their local coordinate systems are shown in Fig. 1 with a tip follower force applied. The elastic deformations in Fig. 1 are exaggerated for clarity. Whereas the e_0 coordinate system coincides with the global coordinate system, the rotation of e_1 is equal to that of the tip point of the first segment. The linear normal modes are calculated in these local systems. To avoid the usage of the normal modes in expressing large rigid-body rotations, these are defined by the rotations of the local coordinate system. Large rigid-body translations, however, are still defined as combinations of rigid-body modes. The elastic deformations relative to the local coordinate system are defined as a linear combination of the elastic normal modes, whereas the rigid-body modes are constrained to yield intersegmental displacement compatibility. To be conveniently consistent with these assumptions, the structural rotations in the following formulation are expressed relative to the local coordinate system. The structural displacements, however, are the total ones, expressed in either the local or global coordinate system.

The modal rigid-body displacements of each segment are constrained to yield displacement compatibility between adjusting

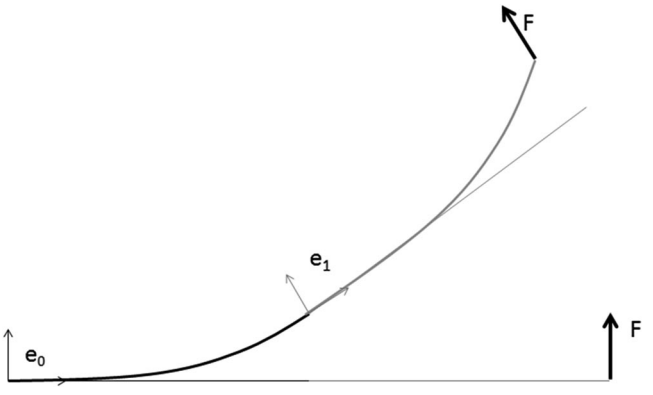

Fig. 1 Structural displacements of two segments and the respective reference frames e_0 and e_1.

structural segments. The master–slave relation between the elastic and rigid-body modes is expressed by means of a transformation matrix $\boldsymbol{T}$ in

$$\xi = \begin{Bmatrix} \xi_r \\ \xi_e \end{Bmatrix} = \boldsymbol{T}\xi_e \tag{2}$$

in which ξ is the full set of mode displacements, ξ_r are the displacements of the rigid-body modes, and ξ_e are the displacements of the elastic modes, as obtained with fictitious masses. Because $\boldsymbol{T}$ depends on large structural rotations, it is nonlinear and time dependent. It is defined later for the case of fixed connections and the case of relative rotations between segments. As both the modal displacements and the transformation matrix are time dependent, the derivatives of Eq. (2) are

$$\dot{\xi} = \dot{\boldsymbol{T}}\xi_e + \boldsymbol{T}\dot{\xi}_e \tag{3}$$

and

$$\ddot{\xi} = \ddot{\boldsymbol{T}}\xi_e + 2\dot{\boldsymbol{T}}\dot{\xi}_e + \boldsymbol{T}\ddot{\xi}_e \tag{4}$$

Equations (2–4) are used to express a reduced set of the modal equation of motion in state-space format:

$$\begin{Bmatrix} \dot{\xi}_e \\ \ddot{\xi}_e \end{Bmatrix} = \begin{bmatrix} \boldsymbol{A} & \boldsymbol{B} \\ \boldsymbol{C} & \boldsymbol{D} \end{bmatrix} \begin{Bmatrix} \xi_e \\ \dot{\xi}_e \end{Bmatrix} + \begin{Bmatrix} 0 \\ [\boldsymbol{T}^T\bar{\boldsymbol{M}}\boldsymbol{T}]^{-1}\boldsymbol{T}^T\phi^T\boldsymbol{F} \end{Bmatrix} \tag{5}$$

with

$$\begin{aligned} \boldsymbol{A} &= 0 \\ \boldsymbol{B} &= \boldsymbol{I} \\ \boldsymbol{C} &= -\left[\boldsymbol{T}^T\bar{\boldsymbol{M}}\boldsymbol{T}\right]^{-1}\left[\boldsymbol{T}^T\bar{\boldsymbol{M}}\ddot{\boldsymbol{T}} + \boldsymbol{T}^T\bar{\boldsymbol{K}}\boldsymbol{T}\right] \\ \boldsymbol{D} &= -\left[\boldsymbol{T}^T\bar{\boldsymbol{M}}\boldsymbol{T}\right]^{-1}\left[2\boldsymbol{T}^T\bar{\boldsymbol{M}}\dot{\boldsymbol{T}} + \boldsymbol{T}^T\bar{\boldsymbol{B}}\boldsymbol{T}\right] \end{aligned} \tag{6}$$

in which $\bar{\boldsymbol{K}}$ and $\bar{\boldsymbol{B}}$ are the generalized stiffness and damping matrices. The terms $\boldsymbol{T}^T\bar{\boldsymbol{K}}\boldsymbol{T}$ and $\boldsymbol{T}^T\bar{\boldsymbol{B}}\boldsymbol{T}$ are diagonal matrices with the generalized stiffness and generalized damping of all segments on the diagonal. $\boldsymbol{F}$ is the vector of discrete time-dependent external forces and inertial forces. The latter are related to the angular velocity of the rotating local coordinate systems, and are neglected in the inertia term of the linear modal formulation, as explained in Sec. II.G.

C. Fixed Connections

Fixed connections are the centerpiece of the current analysis. They are used to rigidly connect the interface of two or more structural segments by establishing displacement compatibility between adjacent blade or wing segments. First, the modes are separated into rigid-body and elastic modes. The rigid-body modal displacements are constrained to establish the displacement compatibility between segments, which yields the transformation of Eq. (2) that can be partitioned as

$$\xi = \begin{Bmatrix} \xi_{1r} \\ \xi_{1e} \\ \xi_{2r} \\ \xi_{2e} \\ \vdots \\ \xi_{nr} \\ \xi_{ne} \end{Bmatrix} = \boldsymbol{T}\begin{Bmatrix} \xi_{1e} \\ \xi_{2e} \\ \vdots \\ \xi_{ne} \end{Bmatrix} \tag{7}$$

in which the subscripts ir and ie denote the rigid-body and elastic modes of the ith segment. For a fixed connection between two adjacent segments without any relative degrees of freedom, $\boldsymbol{T}$ is based on the displacement compatibility:

$$\begin{Bmatrix} \xi_{ir} \\ \xi_{ie} \end{Bmatrix} = \begin{bmatrix} -\phi_{ir}^{-1}\phi_{ie} \\ \boldsymbol{I} \end{bmatrix}\xi_{ie} + \begin{Bmatrix} \phi_{ir}^{-1}\boldsymbol{R}_i\boldsymbol{u}_{i-1} \\ 0 \end{Bmatrix} \tag{8}$$

in which ϕ_{ir} and ϕ_{ie} are rigid-body and elastic modal displacement matrices at the root of the ith segment in local coordinates, and $\boldsymbol{u}_{i-1}$ is a vector of three translations and three rotations of the boundary grid point of the previous segment in the global reference frame. The square rotation matrix $\boldsymbol{R}_i$ converts the six displacements of a grid point from the global reference frame to local coordinates of the ith segment, as defined in Sec. II.D. The vector of boundary displacements at the tip of each segment in global coordinates can be obtained by

$$\boldsymbol{u}_i = \boldsymbol{R}_i^{-1}\phi_{i,\text{end}}\tilde{\boldsymbol{T}}_i\begin{Bmatrix} \xi_{1e} \\ \vdots \\ \xi_{ie} \end{Bmatrix} \tag{9}$$

in which $\tilde{\boldsymbol{T}}_i$ denotes the sequential compatibility transformation matrix for the segment that is considered, as detailed after Eq. (10). The dimension of $\tilde{\boldsymbol{T}}_i$ is k by $i(k-6)$; $\phi_{i,\text{end}}$ is the matrix of modal displacements of the end grid point of the ith segment with dimension 6 by k. As the overall transformation matrix is nonlinear and time dependent, it needs to be constructed at each time step, starting at a known displacement condition. The analysis is carried out sequentially to find the global transformation matrix, starting from a segment with a known displacement. In the presented equations of motion, the structure is clamped at the root of the first segment. Theoretically, it would not be needed to introduce any rigid-body motion for the first segment if the modal reduction of the root segment was carried out with a clamped and a free end. Combining Eqs. (8) and (9) allows assembling the transformation matrix in Eq. (5):

$$\boldsymbol{T} = \begin{bmatrix} \tilde{\boldsymbol{T}}_1 & 0 & 0 \\ [\tilde{\boldsymbol{T}}_2] & & 0 \\ & \vdots & \ddots \\ & [\tilde{\boldsymbol{T}}_n] & \end{bmatrix} \tag{10}$$

in which

$$\tilde{\boldsymbol{T}}_1 = \begin{bmatrix} -\phi_{1r}^{-1}\phi_{1e} \\ \boldsymbol{I} \end{bmatrix}$$

$$\tilde{\boldsymbol{T}}_{i+1} = \phi_{i+1,r}^{-1}\boldsymbol{R}_i\boldsymbol{R}_{i-1}^{-1}\phi_{i,\text{end}}\begin{bmatrix} \tilde{\boldsymbol{T}}_i & -\phi_{ir}^{-1}\phi_{ie} \\ 0 & \boldsymbol{I} \end{bmatrix}$$

As the modal analysis is carried out in a local reference frame, a last step is needed to transform the structural displacements to the displacements in the global coordinate systems, $\boldsymbol{u}_{i,gl}$. In the local coordinate system, the nodal locations of the deformed structure can be obtained by adding the modal displacements to the location vector of the nodes of the finite-element-method model. The global displacement is obtained by integrating the displacements along the structure starting at the root segment:

$$\boldsymbol{u}_{i,gl} = \boldsymbol{R}_i^{-1}\left[\boldsymbol{r}_{\text{undef},i} + \phi_i\begin{bmatrix} -\phi_{ir}^{-1}\phi_{ie} \\ \boldsymbol{I} \end{bmatrix}\begin{Bmatrix} \xi_{ir} \\ \xi_{ie} \end{Bmatrix}\right] + \boldsymbol{u}_{i-1,gl,\text{end}} \tag{11}$$

with

$$\boldsymbol{u}_{0,gl,\text{end}} = 0$$

D. Rotation Matrices in a Corotational Framework

The nonlinear compatibility has been assessed except for the rotation matrix that needs to be used to convert the displacements from the global coordinate system to the body-attached reference frame. The formulation of rotations is one of the key problems in

formulating geometrically nonlinear structural models using a corotational framework. In this paper, total rotations are modeled by the rotational vector approach [21]. First, the coordinate systems are defined by unit-size, orthogonal vectors $\boldsymbol{e}$. In the case of the global coordinate system, the unit vectors $\boldsymbol{e}^g$ are simply the unit vectors of the undeformed coordinate system. For the other coordinate systems, defining unit vectors is slightly more complex. One of the unit vectors is specified based on the undeformed structure. The unit vector is defined along the longitudinal axis of the structure:

$$\boldsymbol{e}_3^i = \boldsymbol{u}_{2,z} - \boldsymbol{u}_{1,z} \tag{12}$$

in which $\boldsymbol{u}$ is the vector of the nodal coordinates of the undeformed structure. The subscript 1, z denotes the location in axial direction of a root boundary grid point, whereas 2, z denotes a position at unit distance along the undeformed beam axis. In the case of the initial coordinate system, without structural deformation, the remaining two unit vectors can be obtained in the same manner. If small strains are assumed and the cross section remains perpendicular to the axis of the tower and blades, this is also true for both the body-attached reference frame and the elastic body-attached reference frame. In the case of large strains and warping, the second and third vectors need to be defined in a different manner. In that case, an auxiliary vector $\boldsymbol{q}_0$ is defined that is orthogonal to $\boldsymbol{e}_3^i$. It is convenient for the blades to specify $\boldsymbol{q}_0$ in the edgewise direction. The vector $\boldsymbol{q}_0$ is normalized to form the second vector of the coordinate system, $\boldsymbol{e}_1^i$. The vectors, $\boldsymbol{e}_3^i$ and $\boldsymbol{e}_1^i$, span a plane, to which a perpendicular vector is computed, which is the third vector of the coordinate system. A sample coordinate system for an undeformed beam is shown in Fig. 2.

$$\boldsymbol{e}_2^i = \boldsymbol{e}_3^i \times \boldsymbol{e}_1^i \tag{13}$$

The orthogonal rotation matrix for a node is obtained using three independent parameters. A vector of rotation angles, Ψ_1 to Ψ_3, each defined around a corresponding direction vector of the body-attached coordinate system, is used to describe the orientation of the segment, based on the global rotations of the previous segment. These rotation angles are used to define a rotation vector $\boldsymbol{u}_r$ and rotation magnitude ψ:

$$\boldsymbol{\Psi} = \begin{pmatrix} \Psi_1 \\ \Psi_2 \\ \Psi_3 \end{pmatrix} = \begin{pmatrix} \boldsymbol{u}_{i,gl}(4) \\ \boldsymbol{u}_{i,gl}(5) \\ \boldsymbol{u}_{i,gl}(6) \end{pmatrix} = \boldsymbol{u}_r \psi \tag{14}$$

in which the rotation magnitude can be obtained from the rotation angles Ψ_1 to Ψ_3

$$\psi = \sqrt{\Psi_1^2 + \Psi_2^2 + \Psi_3^2} \tag{15}$$

Finally, the rotation matrix can be constructed:

$$\boldsymbol{R}_{\text{sub}} = \boldsymbol{I} + \frac{\sin\psi}{\psi}\tilde{\Psi} + \frac{1}{2}\left[\frac{2\sin(\psi/2)}{\psi}\right]^2 \tilde{\Psi}^2 \tag{16}$$

in which $\boldsymbol{I}$ is a unit matrix, and $\boldsymbol{R}_{\text{sub}} = \boldsymbol{I}$ when $\psi = 0$ and

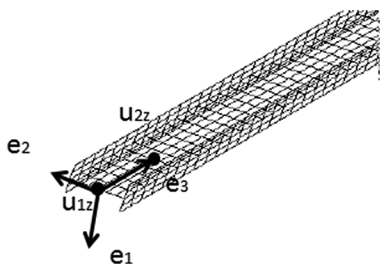

Fig. 2 Sample definition of the coordinate system.

$$\tilde{\Psi} = \begin{bmatrix} 0 & -\Psi_3 & \Psi_2 \\ \Psi_3 & 0 & -\Psi_1 \\ -\Psi_2 & \Psi_1 & 0 \end{bmatrix}$$

As forces, moments, rotations, and displacements need to be transformed into the new reference frame, the full rotation matrix to be used per segment is given by

$$\boldsymbol{R} = \begin{bmatrix} \boldsymbol{R}_{\text{sub}} & 0 \\ 0 & \boldsymbol{R}_{\text{sub}} \end{bmatrix} \tag{17}$$

E. Joints

The formulation of joint connections between segments is an extension of the formulation for fixed connections. Whereas in the case of fixed connections as described earlier, one segment is connected to a previous segment; in the case of a joint, a segment has multiple follower segments. The different follower segments are independent of each other and only attached through compatibility conditions at the joint. An example of such a connection is a helicopter hub that connects multiple blades to one shaft. The compatibility condition for each follower segment with respect to the master segment remains unaltered, as described in Eq. (8). However, the transformation matrix that expresses the relation between the deformation of different segments needs to be modified. Up to the joint, the transformation given in Eq. (10) stays unaltered. After the joint, multiple rows with the same entries in the first positions are added, such that

$$\boldsymbol{T}_{\text{joint}} = \begin{bmatrix} \tilde{\boldsymbol{T}}_1 & 0 & 0 & 0 \\ \tilde{\boldsymbol{T}}_2 & 0 & 0 & \\ \vdots & \vdots & \vdots & \vdots \\ & [\tilde{\boldsymbol{T}}_j] & & 0 \\ & [\tilde{\boldsymbol{T}}_{s1}] & & \\ & [\tilde{\boldsymbol{T}}_{s2}] & & \end{bmatrix}$$

$$\tilde{\boldsymbol{T}}_{s1} = \phi_{j+1,r}^{-1} \boldsymbol{R}_j \boldsymbol{R}_{j-1}^{-1} \phi_{j,\text{end}} \begin{bmatrix} \tilde{\boldsymbol{T}}_j & -\phi_{s1r}^{-1}\phi_{s1e} & 0 \\ 0 & \boldsymbol{I} & 0 \end{bmatrix}$$

$$\tilde{\boldsymbol{T}}_{s2} = \phi_{j+1,r}^{-1} \boldsymbol{R}_j \boldsymbol{R}_{j-1}^{-1} \phi_{j,\text{end}} \begin{bmatrix} \tilde{\boldsymbol{T}}_j & \boldsymbol{0} & -\phi_{s2r}^{-1}\phi_{s2e} \\ \boldsymbol{0} & \boldsymbol{0} & \boldsymbol{I} \end{bmatrix} \tag{18}$$

in which the index j denotes the master segment before the joint, and the indices $s1$ and $s2$ are the follower segments after the joint. This can be easily extended to joints with more than two follower elements. If the slave segment has follower segments by itself, the previously described procedure holds and compatibility is just established with respect to the respective master segment.

F. Morphing Connections

Multiple morphing connections can be found in engineering applications. Examples are the pitch mechanism in wind-turbine blades, or a morphing connection between the aircraft body and the wing. Contrary to fixed connections, morphing connections allow for rotational degrees of freedom. This modifies Eq. (8), which yields

$$\begin{Bmatrix} \xi_{ir} \\ \xi_{ie} \end{Bmatrix} = \begin{bmatrix} -\phi_{ir}^{-1}\phi_{ie} \\ \boldsymbol{I} \end{bmatrix} \xi_{ie} + \begin{Bmatrix} \phi_{ir}^{-1}\boldsymbol{R}_m \boldsymbol{R}_i \boldsymbol{u}_{i-1} \\ 0 \end{Bmatrix} + \begin{Bmatrix} \phi_{ir}^{-1}\boldsymbol{\Omega} \\ 0 \end{Bmatrix} \tag{19}$$

in which $\boldsymbol{R}_m$ is the associated rotation matrix defined in the local reference frame, and $\boldsymbol{\Omega}$ is the displacement vector of the morphing connection

$$\boldsymbol{\Omega} = \begin{Bmatrix} 0 \\ 0 \\ 0 \\ \varphi_1 \\ \varphi_2 \\ \varphi_3 \end{Bmatrix} \tag{20}$$

The variable φ_i denotes the rotations about the principle axes of the body-attached coordinate system of the current segment. These rotation angles are typically given as functions of time. As the morphing rotations do not depend on the elastic modes, Eq. (7) is expanded to include the morphing degrees of freedom:

$$\xi = \boldsymbol{T}\begin{Bmatrix} \xi_{1e} \\ \xi_{2e} \\ \vdots \\ \xi_{ne} \end{Bmatrix} + \begin{Bmatrix} \phi_{11}^{-1}\boldsymbol{\Omega}_1 \\ 0 \\ \phi_{21}^{-1}\boldsymbol{\Omega}_2 \\ 0 \\ \vdots \\ \phi_{n1}^{-1}\boldsymbol{\Omega}_n \\ 0 \end{Bmatrix} = \boldsymbol{T}_{\text{total}}\begin{Bmatrix} \xi_{1e} \\ \xi_{2e} \\ \vdots \\ \xi_{ne} \\ \boldsymbol{\Omega}_1 \\ \boldsymbol{\Omega}_2 \\ \vdots \\ \boldsymbol{\Omega}_n \end{Bmatrix} \tag{21}$$

in which $\boldsymbol{T}_{\text{total}}$ is the transformation matrix $\boldsymbol{T}$, expanded to include the $\boldsymbol{\Omega}$-related terms. This formulation allows the simple application of consecutive morphing connections, by repetitively applying Eq. (19).

G. Applied Forces

Because Eq. (5) is expressed in modal coordinates defined in the local reference frame for each segment, the applied forces in $\boldsymbol{F}$ should be defined in the respective frames. This inherently renders the application of external forces as follower forces, which is very convenient, for example, in aeroelastic analyses, in which the lift and drag forces of a given section are defined with respect to the local coordinate system. Forces that are defined in the global coordinate system should be transformed to local coordinates using the rotation matrices presented in the previous sections.

During simulations with large structural rotations, inertial and gravitational forces play an important role. As modal formulations are used, both need special attention. Being based on small displacements, the generalized inertial forces implied by $\bar{\boldsymbol{M}}$ in Eq. (5) do not account for some discrete acceleration terms resulting from the rotation of the local coordinate systems. Selitrennik et al. [16] identified the missing inertial force terms that should be included in the applied force vector $\boldsymbol{F}$. The rotation-related inertial force vector applied to each mass point is

$$\boldsymbol{f}_\omega = -\boldsymbol{m}\frac{\mathrm{d}\omega}{\mathrm{d}t}\times\boldsymbol{r} - 2\boldsymbol{m}\omega\times\frac{\mathrm{d}\boldsymbol{r}}{\mathrm{d}t} - \boldsymbol{m}\omega\times(\omega\times\boldsymbol{r}) \tag{22}$$

in which ω is the angular-velocity vector of the local coordinate system, and $\boldsymbol{r}$ is the mass location vector in the rotating frame. The three terms in Eq. (22) are the Euler, Coriolis, and centrifugal forces. The assumptions underlying the modal approach already considered the first term. The Coriolis forces $2\boldsymbol{m}\omega\times(\mathrm{d}\boldsymbol{r}/\mathrm{d}t)$ are small for wind-turbine structural dynamics, and thus neglected in this work. However, the centrifugal forces in the last term should be added as external forces [16]. The angular-velocity vector can be directly obtained from the rigid modal velocities given in Eq. (3).

Some forces are expressed in different coordinate systems. Examples of such forces are gravitational forces, which are naturally defined in the global reference frame. Therefore, they need to be converted to the respective local reference frames through the rotation matrices. In these reference frames, the forces can be generalized and included in the equations of motion:

$$\boldsymbol{f}_g = \phi^T\boldsymbol{R}\boldsymbol{g}(\Psi_1,\Psi_2,\Psi_3)\boldsymbol{m}\phi \tag{23}$$

in which $\boldsymbol{g}$ is the gravitational vector, $\boldsymbol{m}$ is the lumped nodal mass, and $\boldsymbol{R}$ is the local rotation matrix. The gravity vector depends on the orientation of the segment in time.

H. Damping

The common approach to include damping into the equations of motion in generalized coordinates uses a diagonal damping matrix, in which the damping values are typically about 2% of the critical modal damping coefficient $B_c = 2m\omega_n$, in which m and ω_n are the generalized mass and the natural frequency of the respective mode. However, when generalized coordinates are based on the modes generated with fictitious masses, the assignment of a diagonal damping matrix $\bar{\boldsymbol{B}}$ in the matrix $\boldsymbol{D}$ of Eq. (7) would effectively cause coupling forces between the natural modes. Hence, it is necessary to define $\bar{\boldsymbol{B}}$, such that it is effectively diagonal, namely, causing no coupling forces when the fictitious masses are removed by Eq. (1) [20]. The process starts with solving the generalized-coordinate eigenvalue problem with the fictitious masses removed:

$$\bar{\boldsymbol{K}}\boldsymbol{\Phi} = \bar{\boldsymbol{M}}\boldsymbol{\Phi}\bar{\omega}_n^2 \tag{24}$$

in which $\boldsymbol{\Phi}$ is the eigenvector matrix, and $\bar{\omega}_n$ is a diagonal matrix with the eigenfrequencies of the new system. The generalized equation of motion could be expressed in the new modal coordinates as

$$\boldsymbol{\Phi}^T\bar{\boldsymbol{M}}\boldsymbol{\Phi}\ddot{\xi}_d + \boldsymbol{\Phi}^T\bar{\boldsymbol{B}}\boldsymbol{\Phi}\dot{\xi}_d + \boldsymbol{\Phi}^T\bar{\boldsymbol{K}}\boldsymbol{\Phi}\xi_d = \boldsymbol{\Phi}^T\phi^T\boldsymbol{F} \tag{25}$$

Whereas the generalized mass and stiffness terms in Eq. (25) are diagonal due to the orthogonal modes, $\bar{B}$ is still to be set, such that the generalized damping matrix will also be diagonal and of the standard form:

$$\boldsymbol{\Phi}^T\bar{\boldsymbol{B}}\boldsymbol{\Phi} = 2\boldsymbol{\Phi}^T\bar{\boldsymbol{M}}\Phi\bar{\zeta}\bar{\omega}_n \tag{26}$$

in which $\bar{\zeta}$ is the assigned diagonal nondimensional damping matrix associated with the modal coordinates of Eq. (25). It is easy to show that, to obtain Eq. (26), $\bar{\boldsymbol{B}}$ should be

$$\bar{\boldsymbol{B}} = 2\bar{\boldsymbol{M}}\boldsymbol{\Phi}\bar{\zeta}\left[\boldsymbol{\Phi}^T\bar{\boldsymbol{M}}\Phi\right]^{-1}\bar{\omega}_n\boldsymbol{\Phi}^T\bar{\boldsymbol{M}} \tag{27}$$

III. Numerical Solver

The following summarizes the terms of the nonlinear state-space equation [Eq. (5)] for cases of fixed connections between the structural segments. It is based on segmental normal modes generated with fictitious masses at the interface coordinates, and expressed in local coordinate systems. The state-space matrices, defined in Eq. (5), include the transformation matrix $\boldsymbol{T}$ that assures interface-displacement compatibility. The discrete external forces, expressed in the local coordinate, are included in $\boldsymbol{F}$. In addition to specific excitation forces, $\boldsymbol{F}$ should also include the centrifugal forces in Eq. (22) and the gravitational forces of Eq. (23), when applicable.

In the numerical examples presented in this paper, the equation of motion, as presented in Eq. (5), is solved using Simulink. The ode23s stiff/mod Rosenbrock's algorithm is used for time integration with a variable step size determined by the algorithm and a relative tolerance of 0.01%. The transformation matrix $\boldsymbol{T}$ is built in every time step starting at root condition. The boundary-grid-point rotation vectors are used to compute the rotation matrix $\boldsymbol{R}$, which is then used for the following segment. This procedure is repeated until the tip of the structure is reached and the full transformation matrix $\boldsymbol{T}$ is obtained. The time derivatives of $\boldsymbol{T}$ are obtained through numerical differentiation. As shown in Eq. (5), the transformation matrix is used to compute the state-space matrix at a given time step. The time derivatives of the state vector are numerically integrated, using a Simulink integrator block for continuous time integration. The resulting state vector at time $t+1$ serves as input to function evaluation at the next time step.

Table 1 Beam properties

Parameter	Value
Web and flange thickness	2 cm
Web height	40 cm
Flange width	20 cm
Elastic modulus	70 GPa
Poisson's ratio	0.3
Density	2600 kg/m^3
Beam length	30 m

IV. Numerical Example: A Uniform Beam

The previously outlined method is applied to a test case to estimate its accuracy and demonstrate convergence for multiple segments. For the presented analysis, a uniform cantilever I-beam is considered. The properties of this beam are given in Table 1.

All structural segments of the test case have been modeled in MSC/Nastran using shell elements. A reference line coinciding with the centroid of the cross section has been added to be used as comparison in the nonlinear simulation. The model has been loaded with fictitious masses at both ends with a diagonal mass matrix consisting of 10^5 kg entries for translational and 10^4 kg $\cdot$ m^2 for rotational degrees of freedom. This model has been created with varying segment lengths, such that it is divided into two, three, four, five, six, eight, and ten segments. The full finite element model was used for verification of the results. The static solution and transient linear simulations were obtained using MSC/Nastran, whereas the static and dynamic nonlinear simulations have been performed with Abaqus. Nonlinear static simulations have been performed with and without follower loads, and compared to the modal-based solution. Figure 3 shows the mesh and the boundary conditions (root clamp) of the Nastran model. Figure 4 provides a close-up of how the forces are introduced into the structure. The total load is split and is applied at the intersection of the flanges and the web. This is done to prevent any twist and to ensure planar deformations.

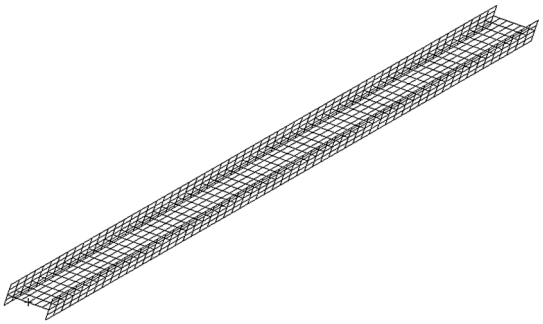

Fig. 3 Nastran model to obtain linear and nonlinear displacements.

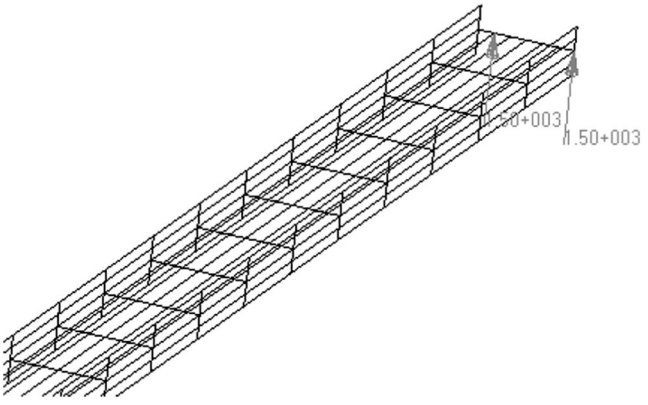

Fig. 4 Zoom in to Nastran model and applied forces.

A. Linear Verification

As a first test case, the presented method is benchmarked against the linear static and dynamic results of the full finite element model of a 20 m version of the beam described in Table 1. The rotation matrix $\boldsymbol{R}_i$, as defined in Eq. (17), is replaced by an identity matrix. For both static and dynamic analyses, a time integration of Eq. (5) was used. The damped-out solution is used as a static comparison. High structural damping coefficients are used to enforce quick convergence of the dynamic simulation to the static results. Figure 5 displays the results due to an applied tip force. One can see that the analytical solution and the solution of the presented approach practically coincide. As a comparison, Fig. 5 also includes the nonlinear solution with the load not following the tip deflection obtained by MSC/Nastran, but remaining in the global coordinate system. The difference between the analytical solution and the results of the mode-shape-based analysis is less than 0.1%.

Figure 6 shows the comparison of the linear time-domain simulation in MSC/Nastran (transient response) and the presented method, both for a step input in force at $t = 0$. Again, the curves correspond very well to each other. Errors are less than 0.1% between two corresponding sets of data points. For the dynamic simulation, Rayleigh stiffness proportional damping was used. Because the modal coupling procedure does not affect the diagonality of the stiffness matrices, the damping matrix remains diagonal and its special treatment in Eq. (27) is not needed.

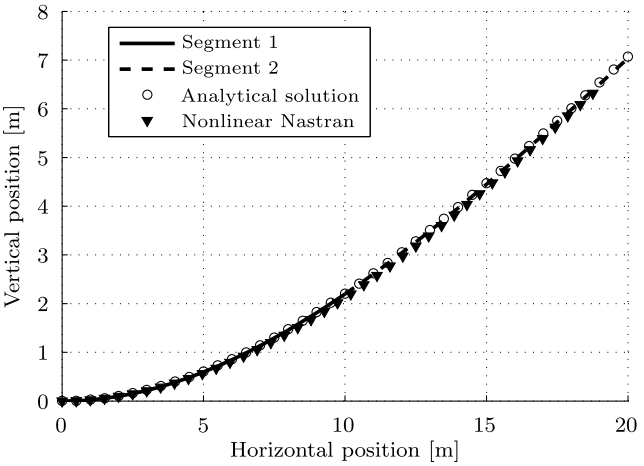

Fig. 5 Linear static analytical solution vs modal simulation, two segments.

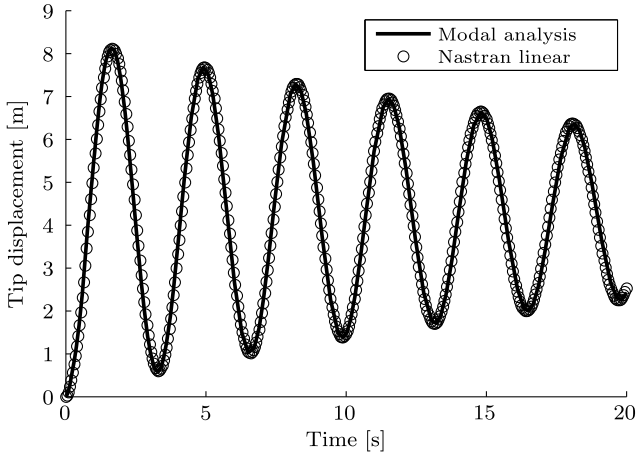

Fig. 6 Linear simulation, Nastran vs modal simulation: response to step in tip load.

B. Nonlinear Static Verification

As the linear modal solutions accurately reproduce the results of the linear finite element analysis, the nonlinear static behavior can be evaluated in the next step. The dynamic analysis has been run, including the nonlinear rotation matrices, until convergence to reproduce the static nonlinear results obtained by Abaqus. The main objective of this chapter was to present a method that offers a compact formulation for nonlinear dynamic solutions with a significant reduction in computation time compared to finite element simulations. The static solution for the Abaqus model takes about 2 min CPU time. Running a dynamic simulation with heavy damping to obtain a static solution with the presented method with two segments only takes of the order of 10 s. This is a speed increase of a factor of 12. Increasing the number of segments will also increase the computational time significantly. A solution with 10 segments for a strongly nonlinear simulation case approaches the same CPU time as the Abaqus simulation.

Figures 7 and 8 show the results for a simulation with two segments. The continuous curve is the computed deformation using the nonlinear modal approach. The figures illustrate the displacement due to a tip force of 2000 and 5000 N, respectively. Both loads are modeled as follower forces in the local reference frame, which is shown in Fig. 1, and follow the rotation and translation of the respective segment. Four static, nonlinear, full finite element simulations have been performed for comparison using Abaqus: a tip force of 2000 and 5000 N both with the load as follower force, and with the tip force in the global coordinate system. The dots represent the linear, analytical solution. Already for two segments, nonlinear effects can be captured by the model. A clear inboard displacement of the beam tip can be observed in the nonlinear modal solution compared to none in the linear solution. Whereas the error in tip defection of the mode-based model with load of 2000 N, compared to Abaqus, is about 1.5%, it is increased to 13% with 5000 N, for highly nonlinear deformations, as shown in Fig. 8.

To improve the accuracy of the nonlinear structural modal model, the number of segments was increased to three. Figures 9 and 10 both show a significant accuracy improvement. The error for 2000 N, in which the tip deflection is 25% of the beam length, is about 0.5%. For the high load of 5000 N, the error in tip deflection is 5%. One can conclude that, in our case, two segments are sufficient for the weakly nonlinear problem, and three segments are needed to obtain good accuracy for the highly nonlinear problem that exhibits tip deflections up to 60–70% of the beam length.

Figure 11 displays an extension of the applicability range of the model. As an example, the rolling up of the beam with an increasing tip moment is considered. At least five segments are needed to model a full circle, because the assumption of linearity for local deformations implies that rotation angles of 90 deg and more cannot be reached for each segment. The result of the simulation with 10 segments is displayed in Fig. 11. Each curve corresponds to the static results due to an applied tip moment increasing from 50,000 to 400,000 N · m in steps of 50,000 N · m. For 10 linear segments, the beam can be completely rolled up, such that its tip touches the root.

C. Nonlinear Dynamic Verification

Two simulations were performed for nonlinear dynamic comparisons: a moderate tip-force step of 1000 N and a high step of 2000 N. Figures 12 and 13 display the time history of tip deflections in the horizontal and vertical directions for the tip-force step of 1000 N. The simulations with both two and three segments closely approximate the deflection amplitude. The frequency of the two-segment analysis is less accurately captured with an error of about 3% compared to the finite element solution. Increasing the

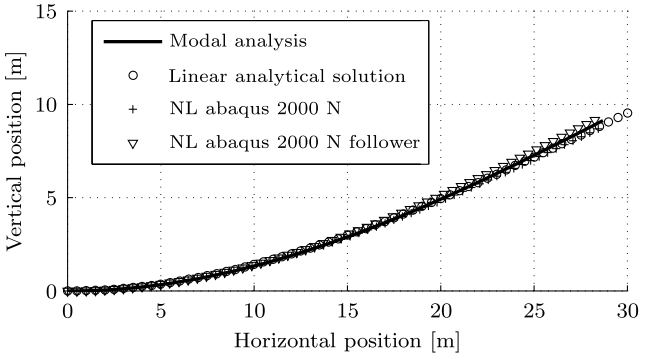

Fig. 7 Static displacement under tip force of 2000 N, two segments.

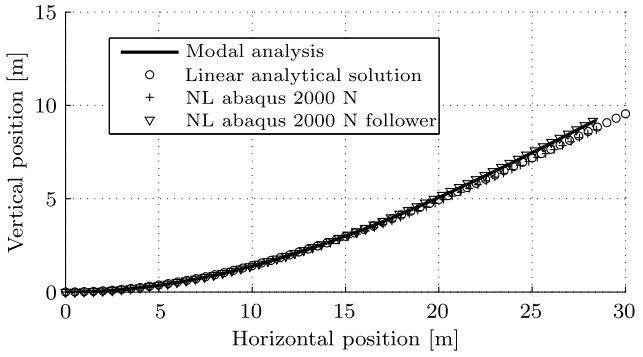

Fig. 9 Static displacement under tip force of 2000 N, three segments.

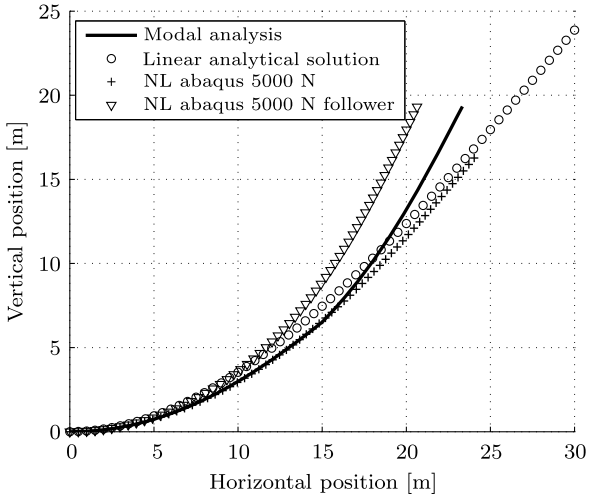

Fig. 8 Static displacement under tip force of 5000 N, two segments.

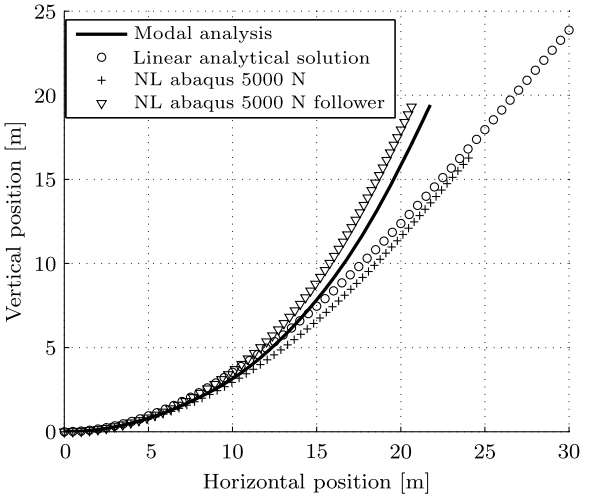

Fig. 10 Static displacement under tip force of 5000 N, three segments.

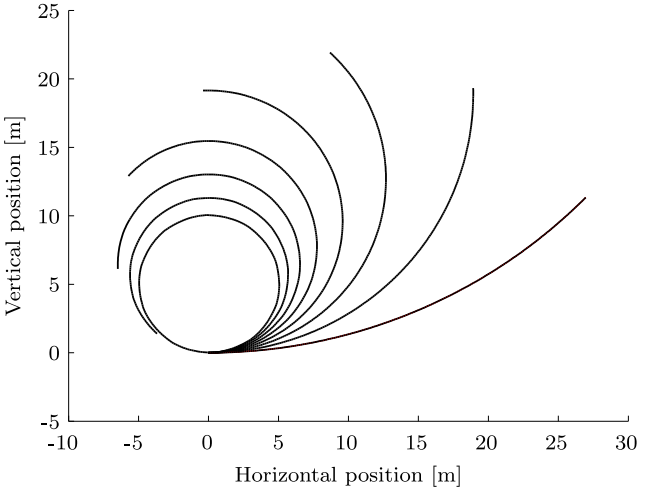

Fig. 11 Static beam deflection with tip moments from 50,000 to 400,000 N · m and 10 segments.

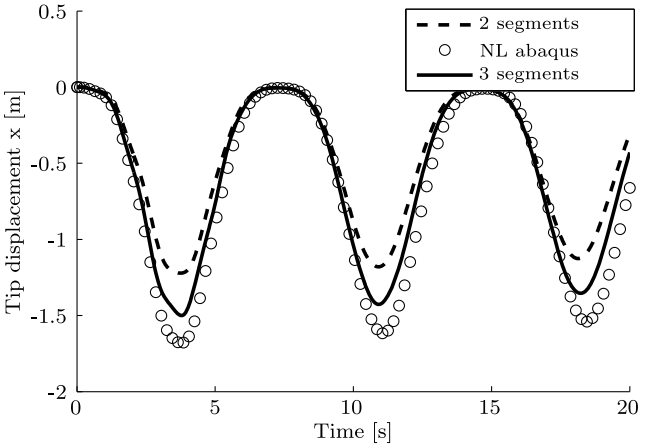

Fig. 12 Horizontal tip displacement for a step tip force of 1000 N.

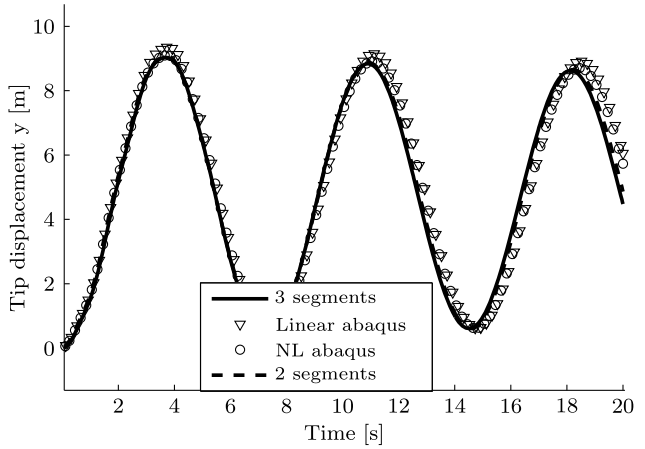

Fig. 13 Vertical tip displacement for a step tip force of 1000 N.

number of segments from two to three improves the simulation, as it reduces the frequency difference between the corotational framework approach and the nonlinear finite element simulation. The reason for the difference in frequency can be found in Fig. 12, which displays the horizontal tip displacement of the beam due to large deflections. Both two and three segments manage to capture the horizontal tip displacement. However, the accuracy of the approach using two segments still needs to be improved by increasing the number of segments in the simulation. Whereas the finite element simulation

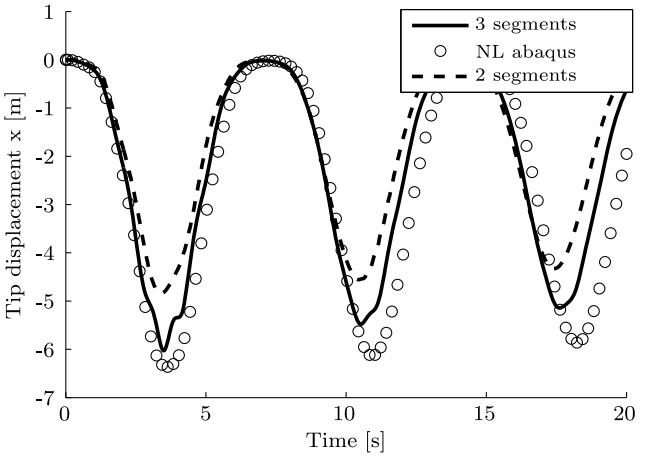

Fig. 14 Horizontal tip displacement for a step tip force of 2000 N.

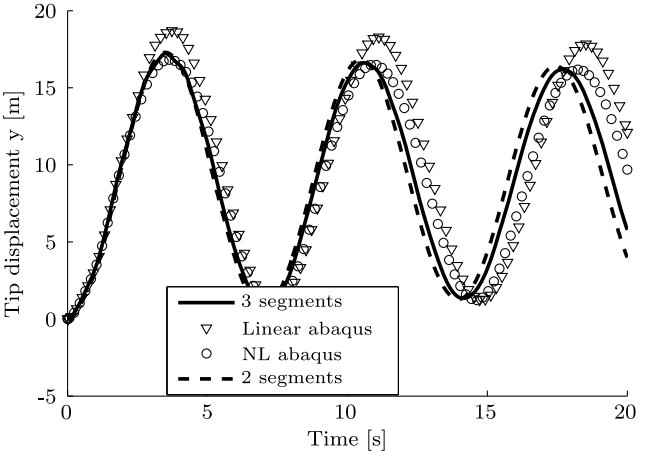

Fig. 15 Vertical tip displacement for a step tip force of 2000 N.

gives a maximal displacement of 1.7 m in the x direction, the simulations with two and three segments show displacements of only 1.2 and 1.5 m, respectively. Increasing the number of segments also improves the prediction of the y-direction tip displacement and the frequency of the response.

Figures 14 and 15 show the results of the same simulations, but with a tip-force step of 2000 N. As expected, the nonlinearity effects are significantly larger. The maximum tip deflection is now more than 60% of the beam length. The simulation using three segments approximates the amplitude of the vertical displacement quite well compared to the finite element simulation, whereas the model using two segments overpredicts the maximum amplitude by about 10%. The vibration frequency is shifted to a higher value, but increasing the number of segments in the corotational framework reduces this difference. The two-segment solution overpredicts the stiffening effect on the frequency by a factor of 2.0 compared to the finite element solution. Increasing the number of segments to three already decreases this difference to a factor of 1.7.

For the tip displacement in the x direction, increasing the number of segments allows approximating the nonlinear finite element solution more accurately. Whereas for two segments, the difference in tip x-direction displacement, as shown in Fig. 14, is around 30%, this difference reduces to 13% for three segments. An undesirable side effect also becomes visible. The solution using three segments produces higher harmonic oscillations, which are damped out after one cycle. These are particularly visible in Fig. 14. The reason for these vibrations is the excitation by a step in tip force, which causes local vibration of the tip segment due to modal truncation. Still, the presented new method captures the x-direction displacements, even for higher vibration amplitudes.

D. Convergence

A static solution was obtained using the modal-based approach with two to ten structural segments. Figures 16 and 17 show the convergence of the tip displacement and the vibration frequency, respectively. For a static tip loading of 2000 N, two segments already give a solution with less than 3% error compared to the finite element solution. When increasing the number of segments, the solution converges quickly to an accuracy that is adequate for most engineering purposes. Four segments yield a solution of less than 0.5% error compared to the Abaqus solution with tip displacements of more than 30% of the beam length. The error for the high-load case of 5000 N is higher and converges slower. Using two segments only gives a very poor representation and produces an error of 13% in terms of tip deflection. When the number of segments is increased, the solution significantly improves to less than 5% error with four segments. When doubling the number of segments again to eight, the error in tip deflection is as small as 2%.

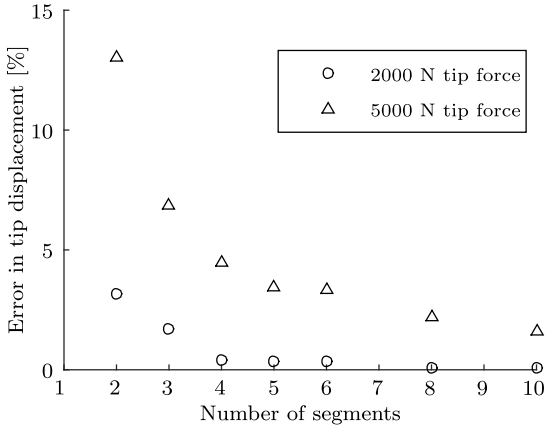

Fig. 16 Error in tip displacement vs number of segments.

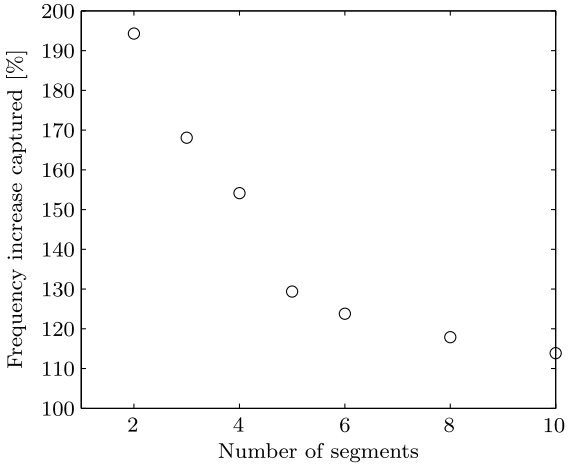

Fig. 17 Frequency increase compared to that of Abaqus vs number of segments.

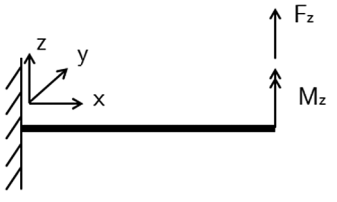

Fig. 18 Structural validation load case of Ibrahimbegovic [22].

Table 2 Beam properties of Ibrahimbegovic [22]

Parameter	Value
Length	10 m
Axial stiffness	10,000 N
Shear stiffness	10,000 N
Torsional stiffness	100 N · m^2
Bending stiffness	100 N · m^2

The geometric nonlinearities introduce a stiffening effect that causes the oscillation frequency to shift from 0.1323 Hz for the linear solution to 0.1396 Hz in case of the nonlinear Abaqus solution. Both cases are determined with a 2000 N step force applied. Because of this large step, the displacement significantly exceeds the static solution and reaches maximum tip displacements of more than 55% of the beam length. As shown in Fig. 17 and may be deduced from Fig. 15, simulations with both two and three segments overpredict the frequency shift by a factor of almost 2.0 and 1.7, respectively. When increasing the number of segments, this overprediction reduces to 17% for eight segments and 13% for 10 elements, resulting in a vibration frequency of 0.1408 Hz compared to 0.1396 Hz in the nonlinear Abaqus solution.

V. Validation of Structural Model with Literature

As an additional validation case, the highly nonlinear beam example of Ibrahimbegovic [22] has been used as benchmark. This is a static example, in which the beam is loaded by a large moment and a force, as shown in Fig. 18. The static loading combination causes the beam to deflect in a helical shape. For the current analysis, a force of 3.5 N and a moment of 14π N · m have been applied. The transformation matrix $\boldsymbol{T}$ is analogous to Eq. (10).

The nonlinear static solution was obtained by pseudotime steps, in which the load was increased. The magnitude of this step in loading was chosen to be 0.2% of the total applied load to ensure converged results. A relaxation scheme with a relaxation factor of 0.2 has been applied, such that the mode displacement of the updated pseudotime step is

$$\xi_{\tau+1} = 0.2 \cdot \xi_{\text{computed}} + 0.8 \cdot \xi_{\tau} \tag{28}$$

in which τ is the pseudotime. During this process, the rotation matrices from the previous pseudotime step were used. A test case with five segments has been performed. For this purpose, the beam properties of Table 2 have been modeled in Nastran using 20 PBEAM elements per segment along the beam axis. The boundary grid points of each segment have been loaded with six concentrated fictitious inertias. The first 20 eigenmodes of each segment, including six rigid-body modes,

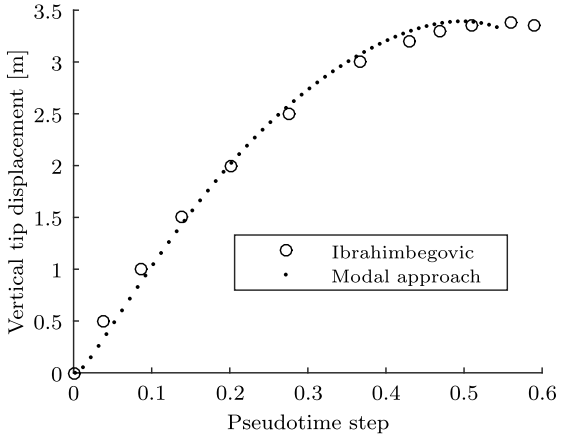

Fig. 19 Out-of-plane tip displacement calculated with five segments compared to Ibrahimbegovic [22].

were taken into account in the analysis. The low number of segments has been chosen intentionally, as to demonstrate the capability of the presented method to model large structural deformations with a small number of degrees of freedom. The result of the static tip displacement in the z direction vs the pseudotime is shown in Fig. 19. The modal approach presented in this chapter and the beam model by Ibrahimbegovic [22] agree well with an error of less than 1% up to a pseudotime of 0.5, which corresponds to an arc of 180 deg combined with the shown out-of-plane tip deflection. The model captures the nonintuitive inversion of the tip displacement starting at about $t = 0.5$, which eventually leads to tip displacements in the opposite direction of the applied force, as has been shown by Ibrahimbegovic [22].

VI. Conclusions

A compact method to describe the geometrically nonlinear structural dynamics of a slender beam has been formulated based on modal reduction. The presented modal approach allows a significant reduction of the structural degrees of freedom with adequate solution accuracy, while still being able to capture geometric nonlinearities. The small-strain assumption of this approach is key to decouple the linear elastic deformation described by the elastic modes and the large deformations introduced by nonlinear compatibility relations in a corotational framework. This decoupling is achieved by dividing the structure into several segments, which are connected to each other by compatibility conditions. Fictitious masses have been introduced at the boundary grid points of the segments to yield local deformations in the low-frequency modes. The representation of the edges in the structural model is instrumental in efficiently constructing the intersegmental compatibility. Even when the structure is modeled with only a few segments, the presented method captures moderate geometric nonlinearities accurately. The model accuracy can be enhanced by increasing the number of segments.

The different compatibility formulations that are related to fixed connections, joints, and morphing connections make the method suitable for a wide range of engineering applications, such as highly flexible aircraft, morphing aircraft configurations, or wind turbines.

Acknowledgment

This research has been funded by the Far and Large Offshore Wind project of the Dutch Ministry of Economic Affairs.

References

[1] Hodges, D., *Nonlinear Composite Beam Theory*, AIAA, Reston, VA, 2006.

[2] Hodges, D. H., "Geometrically Exact, Intrinsic Theory for Dynamics of Curved and Twisted Anisotropic Beams," *AIAA Journal*, Vol. 41, No. 6, 2003, pp. 1131–1137. doi:10.2514/2.2054

[3] Cesnik, C., and Hodges, D. H., "VABS: A New Concept for Composite Rotor Blade Cross-Sectional Modeling," *Journal of the American Helicopter Society*, Vol. 42, No. 1, 1997, pp. 27–38. doi:10.4050/JAHS.42.27

[4] Ferede, E., and Abdalla, M., "Cross-Sectional Modelling of Thin-Walled Composite Beams," *Proceedings of the 55th AIAA/ASME/ASCE/AHS/SC Structures, Structural Dynamics, and Materials Conference*, AIAA, Reston, VA, 2014, pp. 1–36. doi:10.2514/6.2014-0163

[5] Palacios, R., "Nonlinear Normal Modes in an Intrinsic Theory of Anisotropic Beams," *Journal of Sound and Vibration*, Vol. 330, No. 8, 2011, pp. 1772–1792. doi:10.1016/j.jsv.2010.10.023

[6] Palacios, R., Wang, Y., and Karpel, M., "Intrinsic Models for Nonlinear Flexible-Aircraft Dynamics Using Industrial Finite-Element and Loads Packages," *Proceedings of the 53rd AIAA/ASME/ASCE/AHS/ASC Structures, Structural Dynamics, and Materials Conference*, AIAA, Reston, VA, 2012, pp. 1–18. doi:10.2514/6.2012-1401

[7] Hodges, D. H., and Patil, M. J., "Correlation of Geometrically-Exact Beam Theory with the Princeton Data," *Journal of the American Helicopter Society*, Vol. 49, No. 3, 2004, pp. 357–360. doi:10.4050/JAHS.49.357

[8] Dowell, E. H., Traybar, J., and Hodges, D. H., "An Experimental–Theoretical Correlation Study of Non-Linear Bending and Torsion Deformations of a Cantilever Beam," *Journal of Sound and Vibration*, Vol. 50, No. 4, 1977, pp. 533–544. doi:10.1016/0022-460X(77)90501-6

[9] Hopkins, A. S., and Ormiston, R. A., "An Examination of Selected Problems in Rotor Blade Structural Mechanics and Dynamics," *Journal of the American Helicopter Society*, Vol. 51, No. 1, 2006, pp. 104–119. doi:10.4050/1.3092882

[10] Bachau, O., *Flexible Multibody Dynamics*, Springer, New York, 2011.

[11] Bachau, O., Bottasso, C., and Nikishkov, Y. G., "Modeling Rotorcraft Dynamics with Finite Element Multibody Procedures," *Mathematical and Computer Modelling*, Vol. 33, Nos. 10–11, 2001, pp. 1113–1137. doi:10.1016/S0895-7177(00)00303-4

[12] Shabana, A., Hussien, H., and Escalona, J., "Application of the Absolute Nodal Coordinate Formulation to Large Rotation and Large Deformation Problems," *Journal of Mechanical Design*, Vol. 120, No. 2, 1998, pp. 188–195. doi:10.1115/1.2826958

[13] Bachau, O., Betsch, P., Cardona, A., Gerstmayr, J., Jonker, B., Masarati, P., and Sonneville, V., "Validation of Flexible Multibody Dynamic Beam Formulations Using Benchmark Problems," *Multibody System Dynamics*, Vol. 37, No. 1, 2016, pp. 29–48. doi:10.1007/s11044-016-9514-y

[14] Bachau, O., and Laulusa, A., "Review of Contemporary Approaches for Constraint Enforcement in Multibody Systems," *Journal of Computational and Nonlinear Dynamics*, Vol. 3, No. 1, 2007, pp. 1–8.

[15] Bachau, O., and Laulusa, A., "Review of Classical Approaches for Constraint Enforcement in Multibody Systems," *Journal of Computational and Nonlinear Dynamics*, Vol. 3, No. 1, 2007, pp. 1–8.

[16] Selitrennik, E., Karpel, M., and Levy, Y., "Computational Aeroelastic Simulation of Rapidly Morphing Air Vehicles," *AIAA Journal*, Vol. 49, No. 6, 2012, pp. 1675–1686.

[17] De Breuker, R., Abdalla, M., and Gürdal, Z., "A Generic Morphing Wing Analysis and Design Framework," *Journal of Intelligent Material Systems and Structures*, Vol. 22, No. 10, 2011, pp. 1025–1039. doi:10.1177/1045389X11414958

[18] Craig, R. R., and Bampton, C. C., "Coupling of Substructures for Dynamic Analysis," *AIAA Journal*, Vol. 6, No. 7, 1968, pp. 1313–1319. doi:10.2514/3.4741

[19] Karpel, M., and Raveh, D., "Fictitious Mass Element in Structural Dynamics," *AIAA Journal*, Vol. 34, No. 3, 1996, pp. 607–613. doi:10.2514/3.13111

[20] Karpel, M., and Presente, E., "Structural Dynamic Loads in Response to Impulsive Excitation," *Journal of Aircraft*, Vol. 32, No. 4, 1995, pp. 853–861. doi:10.2514/3.46801

[21] Battini, J. M., "Large Rotations and Nodal Moments in Corotational Elements," *Computational Modeling in Engineering and Sciences*, Vol. 33, No. 1, 2008, pp. 1–15.

[22] Ibrahimbegovic, A., "On the Choice of Finite Rotation Parameters," *Computational Methods in Applied Mechanical Engineering*, Vol. 149, Nos. 1–4, 1997, pp. 49–71. doi:10.1016/S0045-7825(97)00059-5

R. K. Kapania
Associate Editor